ResearchGate

See discussions, stats, and author profiles for this publication at: https://www.researchgate.net/publication/222647725

On four highly nonlinear phenomena in wave theory and marine hydrodynamics

Article *in* Applied Ocean Research · October 2002

DOI: 10.1016/S0141-1187(03)00006-3

CITATIONS
37

READS
83

1 author:

John Grue
University of Oslo

67 PUBLICATIONS **1,589** CITATIONS

SEE PROFILE

All in-text references underlined in blue are linked to publications on ResearchGate, letting you access and read them immediately.

Available from: John Grue
Retrieved on: 15 September 2016

ELSEVIER

Applied Ocean Research 24 (2002) 261–274

Applied Ocean Research

www.elsevier.com/locate/apor

On four highly nonlinear phenomena in wave theory and marine hydrodynamics

John Grue*

Department of Mathematics, Mechanics Division, University of Oslo, P.O. Box 1053, Blindern, Oslo 0316, Norway

Received 23 April 2002; accepted 10 May 2002

Abstract

Some recent developments in the formation of extreme waves, kinematics of steep waves, the phenomenon of ringing and currents in the ocean induced by internal waves are reviewed. Formation of extreme waves are simulated by means of a rapid fully nonlinear model. A large wave event taking place in a wave group is characterized by an elevation being significantly larger than the initial amplitude of the group. Recurrence occurs. PIV measurements of Stokes waves exhibit an exponential velocity profile all the way up to the surface elevation (wave slope up to 0.16). The computed velocity profile under crest of an extreme wave corresponds also to an exponential profile. Experimental results of the horizontal force on a vertical circular cylinder in long and steep waves exhibit a secondary cycle of high frequency in the force history. This typically occurs for waves longer than about 10 times the cylinder diameter and a Froude number $\omega\eta_m/\sqrt{gD}$ larger than about 0.4, ω the wave frequency, η_m the maximal elevation, g the acceleration of gravity, D the cylinder diameter. Properties of internal solitons and the induced fluid velocities are described in terms of weakly and fully nonlinear models supported by PIV measurements. A rapid scheme for fully nonlinear interfacial waves in three dimensions is derived, complementing the rapid model of free surface waves.
© 2003 Elsevier Science Ltd. All rights reserved.

Keywords: Wave theory; Ringing; Particle image velocimetry

1. Introduction

This paper reviews some recent results on four topics in wave theory and marine hydrodynamics: formation of extreme waves, kinematics of steep waves, the phenomenon of ringing, and currents in the ocean induced by internal waves. These topics are focussed in an ongoing scientific programme: 'General Analysis of Realistic Ocean Waves' at the University of Oslo. All the topics involve challenges of fundamental character, but needs within maritime, marine and offshore activity give a practical motivation to study the various phenomena. A theoretical-numerical approach is combined with laboratory experiments.

All topics are highly nonlinear. The first topic, formation of very large ocean waves, is studied by means of a transient, fully nonlinear and dispersive model. The model has two essential components: (a) a rapid Laplace equation solver which involves $O(N \log N)$ operations—N the number of computational nodes in the physical space, and (b) a time-stepping scheme where no smoothing is required. The method is significantly faster than previous full methods and is outlined here for three-dimensional motion. Simulations of very large wave events are presented.

In parallel, results are given for the kinematics of the velocity fields induced by steep waves. Laboratory experiments using particle image velocimetry (PIV) are combined with modelling. The velocity profile between the wave crest and the mean sea level is exemplified.

The incoming wave field determines the input parameters to wave analysis of offshore structures. When steep waves interact with offshore platforms being composed by one or several vertical circular cylinders, the wave force may introduce resonant high-frequency vibrations of the platform (ringing). The vibrations are generated by a relatively small high-frequency component of the wave loading. The vibrations appear during a tuned resonant build-up in relatively long and relatively steep waves. A description of the phenomenon together with experimental and theoretical results are given.

The final topic describes currents in the ocean induced by internal waves. This subject is relevant in connection to exploration and exploitation of hydrocarbons or other natural resources in deep water. Risers and cables connecting

* Corresponding author. Tel.: +47-2285-5839; fax: +47-2285-4349.
E-mail address: johng@math.uio.no (J. Grue).

0141-1187/02/$ - see front matter © 2003 Elsevier Science Ltd. All rights reserved.
doi:10.1016/S0141-1187(03)00006-3

floating units on the ocean surface to wells and equipment on the sea floor are exposed to current induced loads. PIV measurements in combination with weakly and fully nonlinear modelling of velocity fields induced by internal waves are described, both for confined and continuous thermocline. Finally, a rapid scheme for fully nonlinear interfacial waves in three dimensions is derived, complementing the rapid model of free surface flows.

The paper is outlined as follows: Models and computations of extreme waves are described in Section 2. Wave kinematics is discussed in Section 3, while the phenomenon of ringing is discussed in Section 4. Nonlinear models of internal solitons and the fully nonlinear transient interface model in three dimensions are described in Sections 5 and 6. Finally, Section 7 gives a conclusion.

2. Extreme waves

Very high waves are reported to appear rather frequently on the ocean surface. Mathematical modelling of the waves is requested. The topic is of high interest within the marine hydrodynamics and offshore engineering communities. Unsolved questions include Under what conditions do extreme waves appear? What is the underlying mechanism of the waves? How frequent are large waves formed? General lack of understanding and appropriate mathematical description of the phenomenon are pointed out. Furthermore, rapid simulation models for wave fields with appreciable size are requested [1,2].

The nonlinear Schrödinger equation or extensions of this equation [3–5] may be applied to investigate large waves at sea. The assumption of a narrow-banded spectrum puts a restriction on the applicability of the models. This is true for the evolution of a general wave field, and for the process taking place in very steep wave events. High-order spectral methods [6–8] are based on Taylor series expansion about a reference level. These are computationally efficient methods. The methods involve high-order derivatives of the wave field, however, which may cause difficulties when the waves are steep. Rather extensive smoothing may be required to continue the simulations.

We here outline another strategy to compute fully nonlinear water waves. The method is derived in Ref. [9] in two and three dimensions. Only the three-dimensional version will be described here. The essential part of the method is a fast converging iterative solution procedure of the Laplace equation. One part of the solution is obtained by Fast Fourier Transform, while another part is highly nonlinear and consists of integrals with kernels that decay quickly in the space coordinate. The number of operations required is asymptotically $\mathcal{O}(N \log N)$, where N is the number of nodes at the free surface. While any accuracy of the computations is achieved by a continued iteration of the equations, one iteration is sufficient for practical computations, while maintaining high accuracy. This results in an explicit scheme. Both partially and fully de-aliased computational schemes with no smoothing or regridding are successfully tested out.

In Section 6, this method is generalized to interfacial flows, for fluid layers of finite thickness.

The method is used to simulate large wave events. In a first example we reproduce simulations of modulated wave trains [10,11], finding either recurrence of the initial state or the rapid onset of wave breaking, depending on the magnitude of the initial steepness. We then proceed one step further as simulations of long wave groups of finite length are performed. Very large wave events take place in the simulations.

2.1. Generalized Dysthe equation

Before proceeding to the fully nonlinear model we describe a most recent generalization of the nonlinear Schrödinger equation [5]. The extended equation in the case of wave propagation on the surface of an infinitely deep ocean reads

$$\frac{\partial B}{\partial t} + \frac{1}{4\pi^2}\int\int_{-\infty}^{\infty} \mathrm{i}[\omega(\mathbf{k}_0+\mathbf{k}) - \omega_0]\mathrm{e}^{\mathrm{i}[\mathbf{k}\cdot(x-y)]}B(\mathbf{y},t)\mathrm{d}\mathbf{y}\mathrm{d}\mathbf{k} + \frac{\mathrm{i}\omega_0 k_0^2}{2}|B|^2 B + \frac{3\omega_0 k_0}{2}|B|^2\frac{\partial B}{\partial x} + \frac{\omega_0 k_0}{2}B^2\frac{\partial B^*}{\partial x} + \mathrm{i}k_0\frac{\partial \bar{\phi}}{\partial x}B = 0, \quad (1)$$

where $\bar{\phi}$ satisfies $\partial\bar{\phi}/\partial y = (1/2)\omega_0\partial|B|^2/\partial x$ at $y=0$, $\nabla^2\bar{\phi} = 0$ for $-\infty < y < 0$, $\partial\bar{\phi}/\partial y = 0$ for $y \to -\infty$. It is assumed that the surface elevation is represented by a modulation of a wave train with a characteristic wavenumber $\mathbf{k}_0$ and a corresponding wave frequency $\omega_0 = \omega(\mathbf{k}_0)$, i.e.

$$\eta(\mathbf{x},t) = \tfrac{1}{2}B(\mathbf{x},t)\mathrm{e}^{\mathrm{i}(\mathbf{k}_0\cdot\mathbf{x}-\omega_0 t)} + \text{c.c.}, \quad (2)$$

where $B(\mathbf{x},t)$ denotes the complex envelope function of the modulation. The linear dispersion relation reads $\omega(\mathbf{k}) = (gk)^{1/2}$, $k = |\mathbf{k}|$, while $\mathbf{x} = (x_1, x_2)$ denotes the horizontal coordinate, y the vertical coordinate, with $y = 0$ in the mean free surface, η the elevation, t time and a star complex conjugate. g denotes acceleration of gravity. Eq. (1) combines a fully linear dispersive behaviour of the waves with cubic nonlinearity of deep water waves. It is noted in Ref. [5] that numerical integration of Eq. (1) can be performed at no additional cost as compared to the nonlinear Schrödinger equation. Eq. (1) provides a useful reference of fully nonlinear simulations of weakly nonlinear and narrow banded wave fields.

2.2. A rapid and fully nonlinear wave model

We here describe the rapid and fully nonlinear wave model developed in Ref. [9]. The method has been developed both in two and three dimensions, and has been fully implemented in the two-dimensional case. The scheme

has also partially been implemented and tested out in three dimensions.

The most essential steps of the method in the three-dimensional case are described here. We consider non-overturning waves in water of infinite depth. (The effect of a finite depth of the water is taken into account later, see Section 6.2.) The method is based on application of potential theory. Let $\phi(\mathbf{x}, y, t)$ denote the velocity potential, and $\eta(\mathbf{x}, t)$, $\mathbf{x}, y$, and t denote surface elevation, horizontal coordinate, vertical coordinate and time, respectively. We introduce the potential function $\tilde{\phi}(\mathbf{x}, t)$ at the free surface determined by $\tilde{\phi}(\mathbf{x}, t) = \phi(\mathbf{x}, \eta(\mathbf{x}, t), t)$ [12]. The kinematic and dynamic boundary conditions at $y = \eta(\mathbf{x}, t)$ give

$$\eta_t - V = 0, \tag{3}$$

$$\tilde{\phi}_t + g\eta + \frac{|\nabla\tilde{\phi}|^2 - V^2 - 2V\nabla\eta\cdot\nabla\tilde{\phi} + |\nabla\eta\times\nabla\tilde{\phi}|^2}{2(1+|\nabla\eta|^2)} + \tilde{p} = 0. \tag{4}$$

In Eqs. (3) and (4) a scaled normal velocity of the free surface, $V = \phi_n\sqrt{1+|\nabla\eta|^2}$, is introduced, where ϕ_n denotes the normal velocity and ∇ the horizontal gradient. p denotes pressure.

Eqs. (3) and (4) may be integrated in time once a relation between η, $\tilde{\phi}$ and V is given. This is obtained by means of the solution of an integral equation which may be derived using Green's theorem, giving

$$\int\int_S \frac{1}{r}\frac{\partial\phi'}{\partial n'}\mathrm{d}S = 2\pi\tilde{\phi} + \int\int_S \tilde{\phi}'\frac{\partial}{\partial n'}\frac{1}{r}\mathrm{d}S, \tag{5}$$

where the potential function, $1/r$, satisfies the Laplace equation in the fluid domain, r is given by $r = [\mathbf{R}^2 + (y' - y)^2]^{1/2}$ and $\mathbf{R} = x' - x$. In Eq. (5), S denotes the instantaneous free surface. Introducing

$$D = (\eta' - \eta)/R, \tag{6}$$

where $R^2 = \mathbf{R}\cdot\mathbf{R}$, Eq. (5) may be written

$$\int\int_{-\infty}^{\infty}\frac{V'}{(1+D^2)^{1/2}}\frac{\mathrm{d}\mathbf{x}'}{R} = 2\pi\tilde{\phi} + \int\int_{-\infty}^{\infty}\frac{-\tilde{\phi}'}{(1+D^2)^{3/2}}\nabla'(\eta' - \eta)\cdot\nabla'\frac{1}{R}\mathrm{d}\mathbf{x}', \tag{7}$$

where the integration is over the (horizontal) $\mathbf{x}'$-coordinate. Alternatively, the equation reads

$$\int\int_{-\infty}^{\infty}\frac{V'}{R}\mathrm{d}\mathbf{x}' = 2\pi\tilde{\phi} + \int\int_{-\infty}^{\infty}(\eta' - \eta)\nabla'\tilde{\phi}'\cdot\nabla'\frac{1}{R}\mathrm{d}\mathbf{x}' + 2\pi T(\tilde{\phi}) + 2\pi N(V), \tag{8}$$

where

$$T(\tilde{\phi}) = \frac{1}{2\pi}\int\int_{-\infty}^{\infty}\tilde{\phi}'[1-(1+D^2)^{-3/2}] \times\nabla'\cdot\left[(\eta' - \eta)\nabla'\frac{1}{R}\right]\mathrm{d}\mathbf{x}', \tag{9}$$

$$N(V) = \frac{1}{2\pi}\int\int_{-\infty}^{\infty}\frac{V'}{R}[1-(1+D^2)^{-1/2}]\mathrm{d}\mathbf{x}'. \tag{10}$$

Solution of Eq. (8) is obtained by application of Fourier transform, giving

$$\mathscr{F}(V) = \mathscr{H}(\tilde{\phi}, \eta) + k\mathscr{F}[N(V)], \tag{11}$$

where

$$\mathscr{H}(\tilde{\phi}, \eta) = k\mathscr{F}(\tilde{\phi}) - k\mathscr{F}\{\eta\mathscr{F}^{-1}[k\mathscr{F}(\tilde{\phi})]\} - \mathrm{i}\mathbf{k}\cdot\mathscr{F}(\eta\nabla\tilde{\phi}) + k\mathscr{F}[T(\tilde{\phi})], \tag{12}$$

$\mathbf{k} = (k_1, k_2)$ denotes the wavenumber in Fourier space with $k = |\mathbf{k}|$, $\mathscr{F}$ denotes Fourier transform and $\mathscr{F}^{-1}$ the inverse transform.

To obtain Eqs. (11) and (12) we first evaluate $\mathscr{F}\{\int\int_{-\infty}^{\infty} V'/R\,\mathrm{d}\mathbf{x}'\} = 2\pi\mathscr{F}\{V\}/k$. Fourier transform of the right of Eq. (8) gives $2\pi\mathscr{F}\{\tilde{\phi}\}$ for the first term and $-2\pi\mathscr{F}\{\eta\mathscr{F}^{-1}[k\mathscr{F}(\tilde{\phi})]\} - 2\pi\mathrm{i}\mathbf{k}\cdot\mathscr{F}(\eta\nabla\tilde{\phi})/k$ for the second term.

2.3. Successive approximations

Eq. (11) is suitable for an iterative solution procedure. Applying the method of successive approximations, we obtain the linear approximation:

$$\mathscr{F}(V^{(1)}) = k\mathscr{F}(\tilde{\phi}). \tag{13}$$

This is used in the analytical integration of the linear part of Eqs. (3) and (4). This step is crucial for a rapid and robust time-stepping method.

An explicit quadratic approximation is given by

$$\mathscr{F}(V^{(2)}) = \mathscr{F}(V^{(1)}) - k\mathscr{F}(\eta V^{(1)}) - \mathrm{i}\mathbf{k}\cdot\mathscr{F}(\eta\nabla\tilde{\phi}). \tag{14}$$

Applying one analytical iteration, an explicit cubic approximation is obtained by

$$\mathscr{F}(V^{(3)}) = \mathscr{F}(V^{(2)}) + k\mathscr{F}[N(V^{(1)})]. \tag{15}$$

In the quadratic approximation, still explicit, we obtain

$$\mathscr{F}(V^{(4)}) = \mathscr{F}(V^{(2)}) + k\mathscr{F}[N(V^{(2)}) + T(\tilde{\phi})]. \tag{16}$$

A continued iteration of Eq. (11) gives a solution to any desired accuracy. We have found that the explicit approximation (16) is useful for modelling waves with local slope even as large as unity, however. The simpler approximation (15) may also be useful for modelling quite steep wave events. A simplified scheme with Eq. (15) is obtained replacing $1-(1+D^2)^{-1/2}$ by $(1/2)D^2$ in Eq. (10), a valid approximation for $|D| \ll 1$. The resulting formula has the advantage that the time-stepping scheme may be

fully de-aliased. We note that the integration over the horizontal plane in Eqs. (9) and (10) may be replaced by an integration over an area with a length scale corresponding to a characteristic length of the waves. This significantly enhances the efficiency of the scheme.

2.4. Simulations of large wave events

In the first example we simulate how a relatively steep, periodic, modulated wave train forms a breaking wave event. This reproduces a finding in Refs. [10,11]. A wave train of the form $A\cos k_0 x$ was in these references perturbed by $\epsilon A\cos((1/n)(n+m)k_0x-(\pi/4))+\epsilon A\times\cos((1/n)(n-m)k_0x-(\pi/4))$. The simulations indicated recurrence to the initial state when the wave slope was moderate. Rapid onset of breaking was found when the wave slope exceeded 0.12, however. Our simulations, with $k_0A=0.22$, $n=8$, $m=1$ and $\epsilon=0.105$, are visualized in Fig. 1. It is seen that Eq. (16) provides a valid approximation to the full Eqs. (11) and (12). In the wave field shown in Fig. 1 the maximal $|\nabla\eta|$ is slightly less than unity. The spectrum of the surface elevation shows a pronounced transfer of energy from moderate to high wavenumbers (Fig. 1(b)). For a slightly later time the waves broke. We note that even Eq. (15) provides a quite useful approximation to the wave field in the example. The shorter wave modes are less well captured using Eq. (15), however.

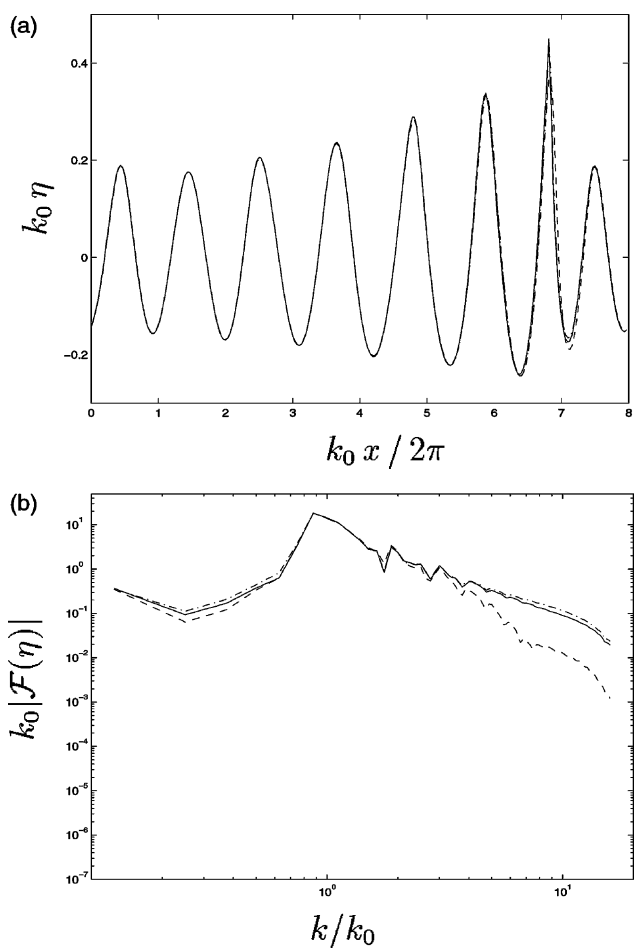

Fig. 1. Wave–wave interaction after 23 periods. (a) η and (b) $\mathscr{F}(\eta)$. Simulations with the two-dimensional version of the model, corresponding to V (Eq. (11)) —, $V^{(4)}$ (Eq. (16)) –·, $V^{(3)}$ (Eq. (15)) – –. Integration in Eqs. (9) and (10) over one wavelength. From Ref. [9], Figs. 5 and 7. Reproduced with permission by J Fluid Mech.

The simulations illustrate that large wave events may occur in an infinitely long train of Stokes waves, provided that the initial slope is sufficiently large. One may then question: can large wave events take place in a wave train of finite length? To answer this question we consider the evolution of a wave train with an initial form as in Eq. (2) with $B(\mathbf{x},0)=A\,\mathrm{sech}[\bar{\epsilon}\sqrt{2}k_0^2A(x-x_0)]$. For $\bar{\epsilon}=1$, this is the exact solution of the nonlinear Schrödinger equation. Longer packets are made by decreasing $\bar{\epsilon}$.

The simulations in Fig. 2, reproduced from Ref. [13], show how an initial wave packet develops in time. In this example $k_0A=0.09$, $\bar{\epsilon}=0.26$. Integration of the 2D versions of Eqs. (9) and (10) is over one wavelength. After a while, a very large wave event takes place in the group, slightly ahead of the center of the group. The wave elevation is as large as about three times the initial wave amplitude. A significant portion of the wave energy is transferred to high wavenumbers during the event, but is returned to the main part of the wave spectrum afterwards, indicating that a recurrence is taking place. Large wave events also take place at later times. The initially long wave packet is seen to disintegrate into three wave groups, with slowly varying amplitudes being envelope solitons. The simulations show that the two leading solitons continuously interact, producing large wave events quite regularly. A third small soliton is found to have less interaction with the two leading ones (results not shown). We have also performed computations integrating the extended Dysthe equation (1). The latter produces the first large wave event in Fig. 2, with a somewhat smaller peak than observed here (results not shown). In our simulations, Eq. (1) ceases to be valid for times when $\omega_0t/2\pi$ exceeds 200, approximately, ω_0 the wave frequency. This corresponds to $(k_0A)^3\omega_0t$ exceeding unity. Simulations using the full method and Eq. (1) become fundamentally different. The relaxed assumption of a narrow-bandedness of the spectrum is an advantage with the full method as compared to Eq. (1). (Simulations with the nonlinear Schrödinger equation diverges from the full solution when $(k_0A)^2\omega_0t$ exceeds unity.)

3. Kinematics of waves

The kinematics of steep ocean waves receives a continued interest within offshore and coastal engineering [14,15]. The kinematics of the waves determine the input parameters to analyze sea loads on ships, offshore platforms and other installations in the marine environment. Valid

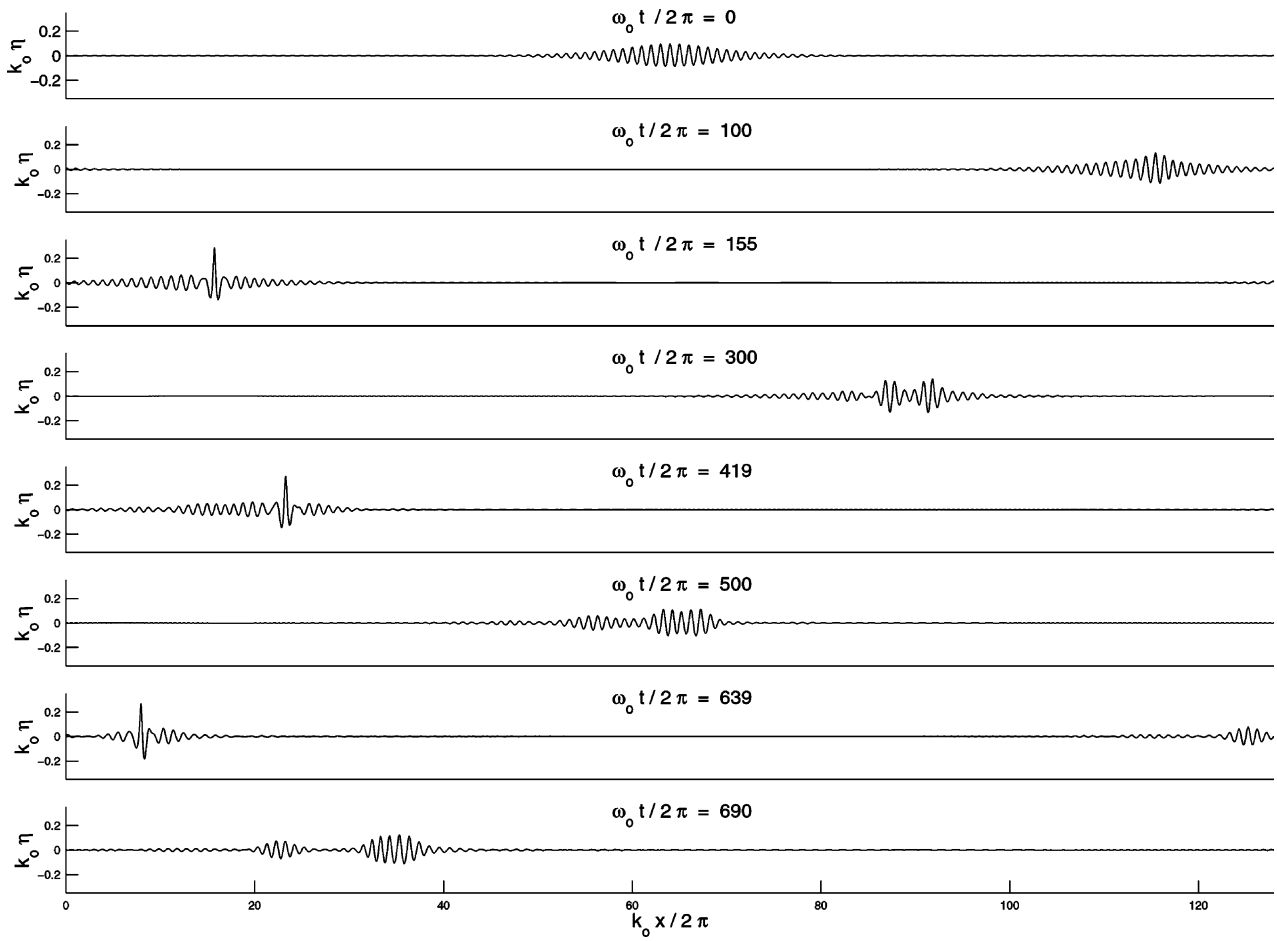

Fig. 2. Formation of large wave events. Simulations with the two-dimensional version of the model, corresponding to $V^{(4)}$ (Eq. (16)). Computational domain with 128 wavelengths, resolution 32 nodes per wavelength, $k_0A = 0.09$, $\bar{\epsilon} = 0.26$. Infinite water depth. From Ref. [13, Fig. 2].

computations of the wave loads therefore depend on reliable predictions of the wave field and the wave kinematics.

We shall here consider two examples. The first one describes the velocity field in a periodic wave train. Precise Stokes waves are generated in a wave tank [16, Section 3]. The actual wave slope is $kA = 0.16$, k the wavenumber, A the wave amplitude. In this case the wave induced fluid velocities may also be determined theoretically by the gradient of the velocity potential $(Aig/\omega)e^{ky+i(kx-\omega t)} \times (1 + O(kA)^3)$, where real part is understood, and $\omega^2 = gk(1 + (kA)^2)$. Wave propagation is along the x-direction. Particle Image Velocimetry (PIV) of the wave field is obtained [17, 18]. The field of view corresponds to a quarter of the wavelength in the horizontal direction and a fifth of the wavelength in the vertical direction. The wave induced velocity field $\mathbf{v} = (u, v)$, u the horizontal velocity and v the vertical, is normalized by Agk/ω, where A and ω are recorded in the experiments and k is obtained from the nonlinear dispersion relation. The non-dimensional velocity $|\mathbf{v}|/(Agk/\omega)$ is plotted in Fig. 3(a) for all obtained velocity columns in the field of view in the experiment (all horizontal positions). A remarkable correspondence with the exponential profile is evident for the whole water column, even above the level of the mean free surface.

In the second example we obtain the velocity profile under crest of a large wave event similar to the first one as shown in Fig. 2. In this case we identify from the wave record (at a fixed point) the (local) trough-to-trough period T_{TT} and the maximal elevation η_m of the event. The local wave frequency is determined by $\omega = 2\pi/T_{TT}$. The local wave slope, ϵ_0, and the wavenumber, k, are estimated from $\omega^2/(gk) = 1 + \epsilon_0^2$, $k\eta_m = \epsilon_0 + (1/2)\epsilon_0^2 + (1/2)\epsilon_0^3$. The velocity profile under crest is visualized in Fig. 3(b). Together with the fully nonlinear computations is included the exponential (linear) profile. A good correspondence between the two non-dimensional velocity profiles is found. The scaling of the horizontal velocity is chosen as $\epsilon_0\sqrt{g/k}$.

We are currently investigating the wave kinematics comprising velocity fields in focussing waves, irregular waves, the leading transient part of a wave field, and in large wave events due to the evolution of a wave group. Experimental PIV studies are combined with theoretical modelling.

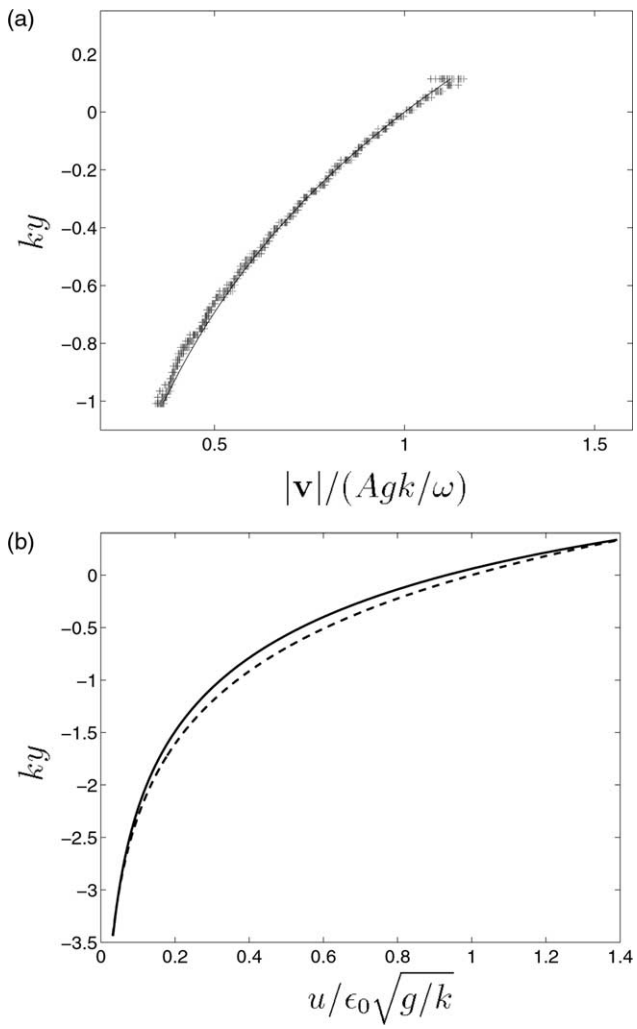

Fig. 3. Profile of the horizontal velocity at the wave crest. (a) Stokes waves with $kA = 0.16$ and $kh = 4.9$ (h the water depth). ' + 'velocity measurements using PIV, taken from 20 columns of velocity field at the wave crest crest. exp(ky) : —. Reproduced with permission by Exp Fluids. (b) Velocity profile in extreme wave with $k\eta_m = 0.34$. Fully nonlinear computations: — exp(ky) : – –. Infinite water depth. k and ϵ_0 are defined in the text.

4. Ringing

Standard computer codes for wave analysis of ships and offshore structures are based on linear and second-order wave diffraction–radiation models [19,20]. The analysis tools provide good predictions of the wave loads in the main part of the wave spectrum. High-frequency wave loads occuring in high sea states have in recent years been identified, however. These are not modelled by the standard analysis tools. The high-frequency loads are typically excited on tension-leg platforms or gravity based platforms which are constructed from one or more vertical cylinders. The high-frequency loads may generate vibrations at the resonance period of the structure. This period may be up to a few seconds. The generation of the high-frequency responses is characterized by a resonant build-up during a time interval of the order of one wave period and is termed 'ringing', due to its sudden appearance. Resonant ringing motion was first observed in wave tank experiments [21], see Fig. 4, but is also observed in large scale [22]. Ringing induced loads may be a concern with regard to fatigue and is a problem that should be avoided.

The phenomenon of ringing has motivated several theoretical and experimental studies. The experimental studies have been carried out in wave tanks with incoming focussing wave groups and steep random waves [23–27] and with incoming periodic waves [16]. The primary focus of the theoretical studies have been to capture the components of the wave force up to the third harmonic wave frequency [28,29]. A fully nonlinear model has also been developed [30].

In the first step it is instructive to consider the wave force when the incoming waves are periodic Stokes waves. In this case the incoming velocity field is oscillating with the fundamental wave frequency only. The higher harmonic wave forces are then caused by the interaction between the wave field and the cylinder. In the experiments [16] the incoming waves had a slope up to $kA = 0.24$, k the wavenumber, A the wave amplitude. The non-dimensional

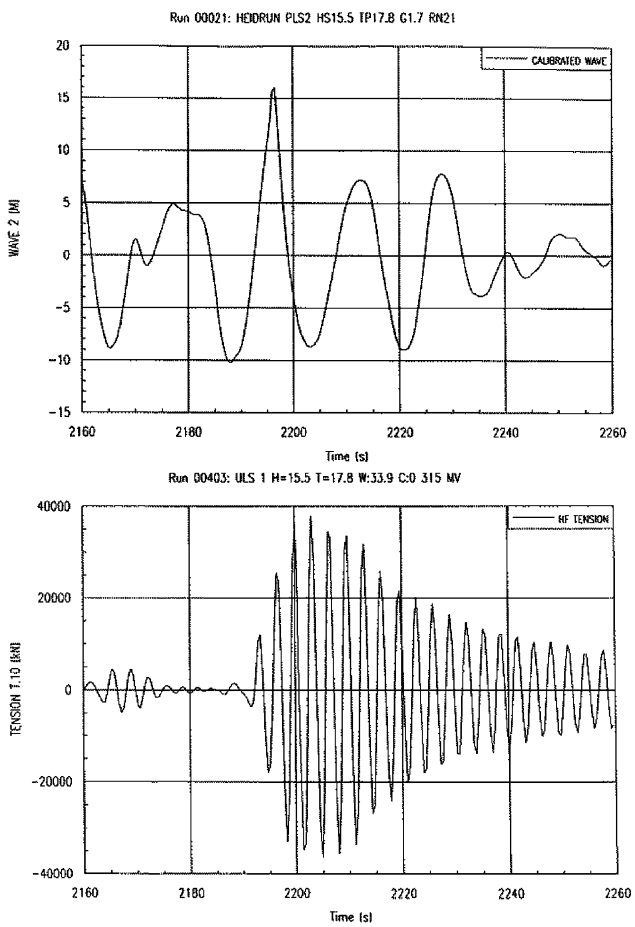

Fig. 4. Resonant build-up of vibrations in model tests. High-frequency tension in tether of the Heidrun TLP (lower figure), elevation of calibrated waves (upper figure). (Ringing report [21]). Reproduced with permission by Statoil.

wavenumber was in the range $0.166 < kR < 0.378$, R the cylinder radius. The first seven harmonics of the horizontal wave force were measured, i.e.

$$F(t) = \mathrm{Re}(F_1 e^{i\omega t} + F_2 e^{i2\omega t} + F_3 e^{i3\omega t} + \cdots + F_7 e^{i7\omega t}), \qquad (17)$$

and were compared to theoretical predictions when possible.

The main findings in Ref. [16] may be summarized by: The measured first harmonic force compare well with the Morison equation, or alternatively the (linear) McCamy-Fuchs solution, for small, moderate and large wave slope, even for kA up to 0.24. The fundamental force component is predominate. The second and third harmonic forces are well predicted by perturbation models, for small and moderate wave slope (kA), but decay from the theoretical predictions for large kA. The measured second-, third- and fourth harmonic forces all become of comparable size when the wave amplitude becomes comparable to the cylinder radius (Fig. 5). The force components F_5, F_6, F_7 are then somewhat smaller. The total super harmonic part of the force becomes about 10% of the fundamental, when the wave amplitude is comparable to the cylinder radius.

The high-frequency resonant vibrations in the model tests of the Heidrun and Draugen platforms took place with a non-periodic wave input. This motivated us to set up laboratory experiments where a focussing incoming wave group gave a large wave event at the location of the cylinder. The signal driving the wave maker had in these experiments a fixed time history but was multiplied by an amplitude factor. The latter was varied stepwise from a small value, producing a linear wave, to a large value, producing a breaking wave close to the position of the cylinder. The resulting wave force was found to be oscillating with the incoming acceleration field of the waves, for small and moderate wave slope. Beyond a threshold amplitude, a pronounced secondary and relatively rapid force cycle appeared in the force history, however (Fig. 6). This secondary cycle had a magnitude of about 10% of the peak-to-peak force and a period of about 15% of wave period. Its resultant force was found to be acting slightly below the mean water line of the cylinder [23,24].

A sharp force maximum like the one seen in Fig. 6 may lead to a build-up of resonant motions of a marine structure. The presence of a secondary force cycle may significantly enhance such a build-up.

Several force measurements have been carried out for various incoming wave fields. The wave forces in steep transient wave groups exhibit in a systematic way the same behaviour as visualized in Fig. 6 [31]. The appearance of the secondary force cycle depend both on the relative cylinder radius and the relative wave amplitude. Here this appearance is plotted as function of the incoming wavelength relative to the cylinder diameter and the magnitude of the fluid velocity induced by the wave, $\omega\eta_m$, non-dimensionalized by $\sqrt{gD}$. η_m denotes the maximal elevation of the incoming wave at the cylinder position and $D = 2R$ the cylinder diameter (Fig. 7). Results from other investigations are also included [21,25,26,32].

We observe that the secondary force cycle takes place when the wavelength is more than 10 times longer than the cylinder diameter and when the Froude number, $\omega\eta_m/\sqrt{gD}$, is larger than about 0.4, roughly speaking. The boundaries are not entirely sharp.

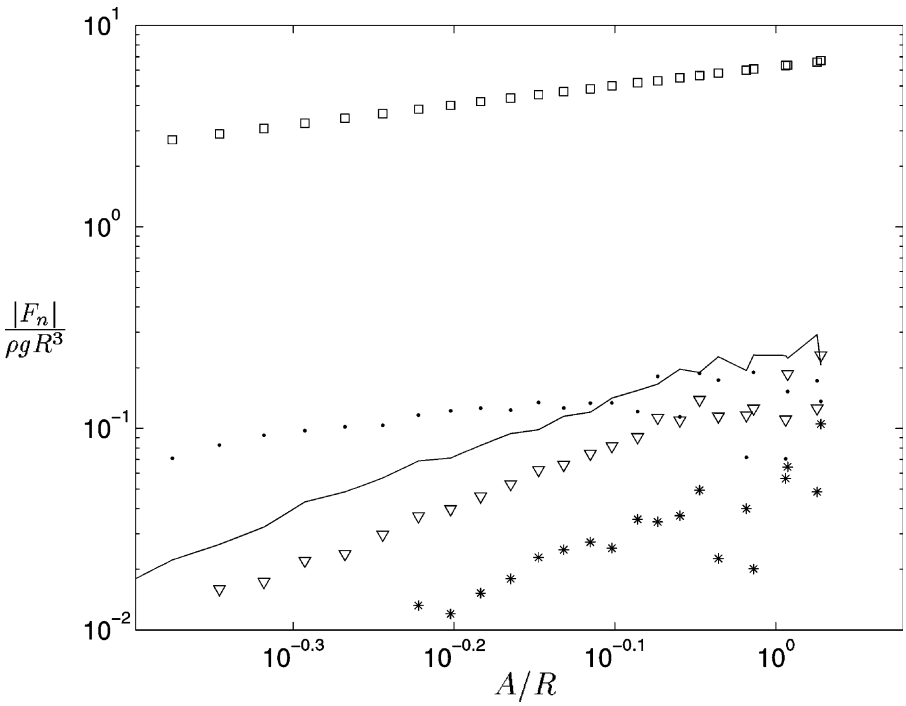

Fig. 5. Harmonic components of the wave force, see Eq. (17). $|F_1|$ (squares), $|F_2|$ (dots), $|F_3|$ (solid line), $|F_4|$ (triangles), $|F_5|$ (stars). $kR = 0.245$. (ρ density, g acceleration of gravity, R cylinder radius.) Data are reproduced from Ref. [16].

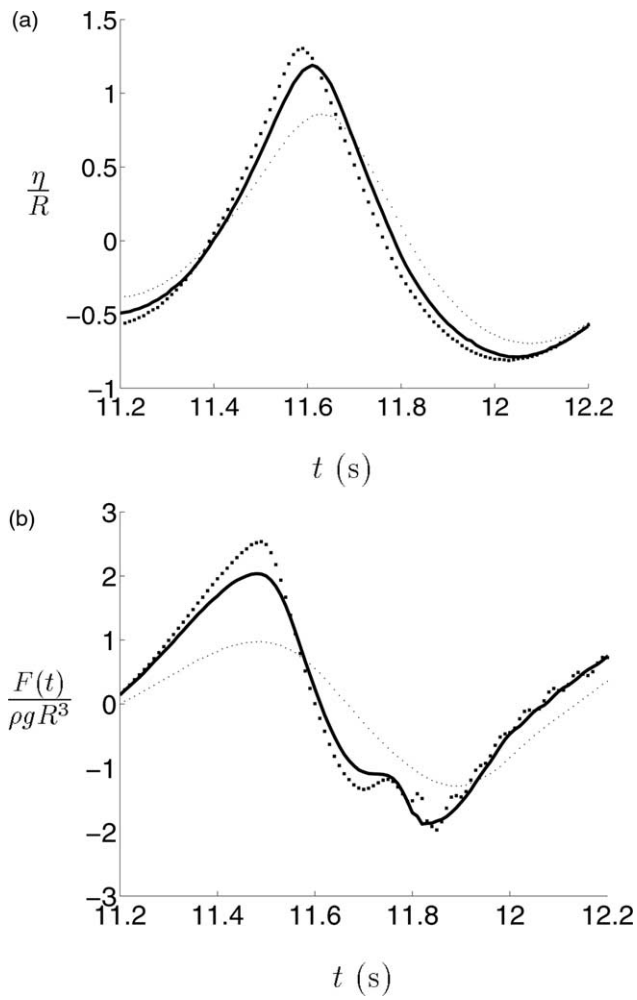

Fig. 6. Horizontal wave force on a vertical cylinder in focussing waves. (a) Elevation at the cylinder position, with $k\eta_m = 0.23$ (thin dots), 0.33 (solid line), 0.37 (thick dots). (b) Corresponding non-dimensional force on the upper force transducer (corresponding to the moment with respect to the bottom of the cylinder). $kR = 0.27–28$. $R = 6$ cm.

We have in the laboratory observed that the presence of a secondary load cycle in wave tank experiments of moderate scale may not be reproduced when the scale becomes too small. This may be explained by occurrence of flow separation. The onset of the latter takes place for a smaller wave amplitude in experiments with small scale than in larger scale. This depends on the value of the β-number ($= D^2/\nu T$, ν the kinematic viscosity, $T = 2\pi/\omega$) [33]. We argue that this is the reason why a secondary load cycle is not indicated in Fig. 7, for λ/D around 25–30 and Froude number around 0.5–0.6.

We note that the value of $\omega\eta_m$ indicates the magnitude of the local quasi-steady current due to the wave. A Froude number of 0.4 corresponds to a free wave with length $2R$, on the local quasi-steady current at the cylinder. We speculate if the secondary force cycle is due to a particular resonance between the cylinder and the induced local flow at the cylinder.

In any case, the results in Fig. 7 indicate when pronounced higher harmonic wave loads on a vertical circular cylinder take place, and thereby when ringing may occur.

The theoretical third harmonic models [28,29] may be appropriate when $\omega\eta_m/\sqrt{gD}$ is larger than about 0.4 and λ/D is larger than about 10. The models may significantly overestimate loads at high frequency when $\omega\eta_m/\sqrt{gD}$ is smaller than about 0.4 and when $\lambda/D < 10$, however.

5. Internal solitons

Internal waves may propagate in a stratified ocean. A prominent example is internal solitons travelling along the thermocline. (The term soliton is here used in a generalized sense.) Internal solitons in the ocean occur very frequently [34,35]. The waves may attain very large amplitudes. Solitons in the Celtic Sea with almost maximal amplitudes are documented [36]. Excursions of the thermocline of up to four times the surface layer thickness are observed on the Oregon Shelf [37]. The wave propagation transport water masses, sediments and other particles. Slowly varying currents of appreciable magnitude are induced in the ocean due to internal waves, in a range that typically may be less than about 0.5 m s^{-1}. Velocities larger than 1 m s^{-1} are documented, however. When the thermocline is relatively thin, the motion may mathematically be described by a two-layer model. The thin thermocline is then replaced by an interface separating the upper and lower fluid. Below we outline weakly and fully nonlinear interfacial wave models including examples. Wave propagation in a fluid with a linearly stratified upper layer is also briefly commented on.

5.1. Korteweg-de vries model

Nonlinear interfacial wave models may be obtained from the weakly nonlinear Boussinesq equations or the Korteweg-de Vries (KdV) equation [38,39]. The two-layer model has an upper layer of density ρ_2 and thickness h_2 and a lower layer of density ρ_1 and thickness h_1. The KdV equation modelling the vertical excursion η of the interface reads

$$\frac{\partial \eta}{\partial t} + c_0 \frac{\partial \eta}{\partial x} + \alpha\eta \frac{\partial \eta}{\partial x} + \beta_0 \frac{\partial^3 \eta}{\partial x^3} = 0, \tag{18}$$

where x denotes the horizontal coordinate and

$$c_0 = \left(\frac{g' h_1 h_2}{h_1 + h_2}\right)^{1/2}, \qquad \alpha = \frac{3}{2} c_0 \frac{h_2 - h_1}{h_1 h_2},$$

$$\beta_0 = \frac{1}{6} c_0 h_1 h_2, \qquad g' = g(\rho_1 - \rho_2)/\rho_1.$$

In the expressions above, the Boussinesq approximation is made, assuming that the density difference is small, i.e. $(\rho_1 - \rho_2)/\rho_1 \ll 1$. The soliton solution in the case of

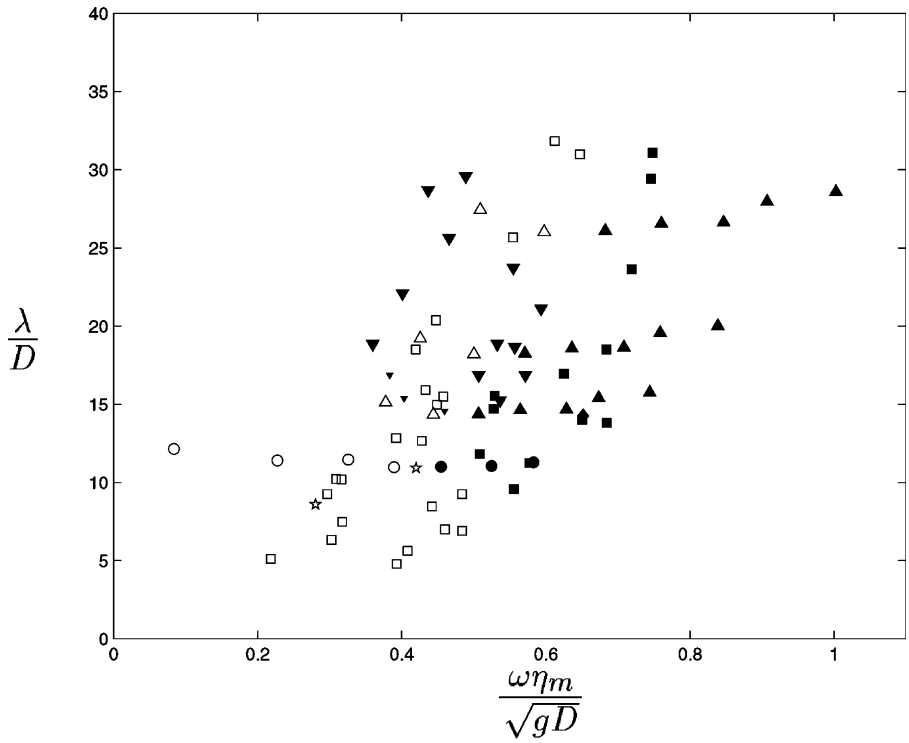

Fig. 7. Filled symbols indicate presence, and open symbols absence, of a secondary load cycle in the force history. Our results, with cylinder radius $R = 3, 4$ cm (squares), [32] $R = 16.4$ cm (downward pointing triangle—small triangle means less pronounced effect), [26] $R = 6.4, 5, 3.5$ cm (upward pointing triangle), [25] $R = 15.6$ cm (pentagram), [21], result for Draugen $R = 16.4$ cm (diamond), [23] $R = 6$ cm (circle).

a depression wave, occurring when $\rho_2 h_1^2 - \rho_1 h_2^2 > 0$, reads: $\eta(x,t) = -A\ \mathrm{sech}^2[(x - ct)/\lambda]$, where the nonlinear wave speed is given by $c/c_0 = 1 + (1/2)A(h_1 - h_2)/(h_1 h_2)$ and the wavelength by $1/\lambda^2 = (3/4)A(h_1 - h_2)/(h_1^2 h_2^2)$. KdV theory for long waves and amplitude up to about 0.4 times the depth of the thinner layer has been experimentally confirmed [40–43].

5.2. The Benjamin-Ono equation

Weakly nonlinear internal waves, in the case with one of the layers being infinitely thick, were investigated, finding solitons of algebraic form [44]. Later, an unsteady behaviour of the motion was included [45], arriving at an equation, termed the Benjamin-Ono (BO) equation, i.e.

$$\frac{\partial \eta}{\partial t} + c_0 \frac{\partial \eta}{\partial x} + \alpha\eta \frac{\partial \eta}{\partial x} - \frac{1}{2} c_0 h_2 \mathrm{PV} \frac{1}{\pi} \int_{-\infty}^{\infty} \frac{\eta_{x'x'}(x',t)}{x - x'} \mathrm{d}x' = 0, \tag{19}$$

where PV denotes principal value, $c_0 = (g' h_2)^{1/2}$ and $\alpha = -(3/2)c_0/h_2$. Solutions of Eq. (19) (and Eq. (18)) are conveniently obtained using, e.g. Fourier transform, giving for Eq. (19) $\mathscr{F}(\eta)_t + \mathrm{i}kc_0\mathscr{F}(\eta) + (1/2)\mathrm{i}k\alpha\mathscr{F}(\eta^2) - (1/2)\mathrm{i}k|k|h_2 c_0 \mathscr{F}(\eta) = 0$. The soliton solution of Eq. (19) reads: $\eta(x,t) = -A/(1 + [(x - ct)/\lambda]^2)$, where $c/c_0 = 1 + (3/8)A/h_2$ and $\lambda = (4/3)h_2^2/A$.

It appears that Eq. (19) is a valid model for A/h_2 up to about 0.1–0.2. The 'finite-depth theory' [46,47] bridges the gap between the KdV and the BO-equation, but has significantly less range of validity than the KdV equation. The relations between the various solution parameters in the KdV, BO and the intermediate depth long wave equations were discussed in Ref. [48].

5.3. Fully nonlinear solitons

Several works on modelling fully nonlinear internal solitons have been published during the last couple of decades [49–51]. We shall here show fully nonlinear computations of interfacial solitons using the method described in Ref. [43, Section 3.1]. The main steps of the method include waves of permanent form are modelled in the frame of reference moving with the wave. The velocity field of the two-layer fluid is expressed in terms of complex analysis. Integral equations for the velocity field in the upper and lower fluid are derived using Cauchy's integral theorem. The kinematic and dynamic boundary conditions close the set of equations determining the velocity field and the nonlinear wave speed. The model is coded in MatLab and may be downloaded [52].

Fully nonlinear computations of the excess speed $c/c_0 - 1$ compare well with the KdV model, for moderate amplitude. The fully nonlinear computations are confirmed by laboratory measurements using particle tracking velocimetry and PIV (Fig. 8(a)). The predicted and measured wave profiles exhibit a corresponding agreement (Fig. 8(b)). The KdV model is less good when $A/h_2 = \mathcal{O}(1)$, however.

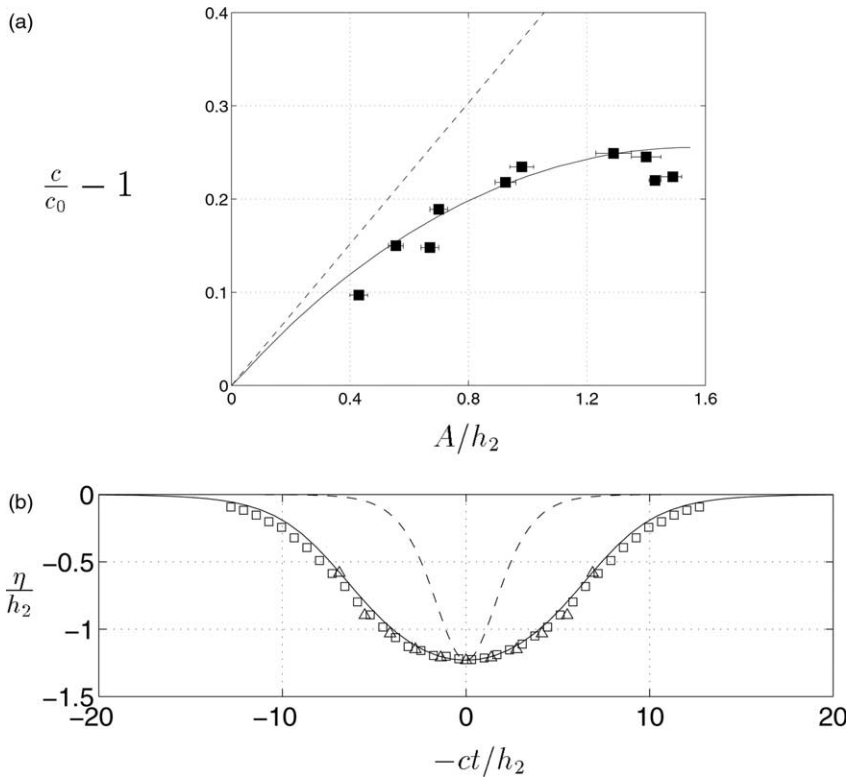

Fig. 8. (a) Excess speed. (b) Wave profile. Fully nonlinear computations (solid line), KdV model (dashed line) and experiments (squares and triangles). $h_1/h_2 = 4.13$. From Ref. [43, figures 6 and 7d]. Reproduced with permission by J Fluid Mech.

Examples of the wave induced horizontal velocity profile, obtained at the maximal excursion of the soliton, are visualized in Fig. 9. The first profile is due to a soliton in a two-layer fluid with constant density in each of the layers (Fig. 9(a)). In the second example (Fig. 9(b)) the upper shallow fluid layer has a linear stratification, while the deep lower layer has constant density. The induced fluid velocity may in the latter case become comparable to the wave speed, even for a moderate wave amplitude [53].

The vertical average of the horizontal fluid velocity induced in the layers, $\bar{u}$, may be determined from conservation of mass. For the thinner (upper) layer we obtain $\bar{u}_2 = c\eta/(h_2 + \eta)$.

6. Transient interface model in three dimensions

Fully nonlinear transient computations of internal waves are few. Steadily progressing interfacial waves were simulated in Ref. [54] while interfacial waves and roll up of vortices developing from an initial disturbance were computed in Ref. [55]. The formation of large amplitude interfacial bores and solitons in transcritical flows at topography were studied in Ref. [56] deriving a fully nonlinear and transient scheme in two dimensions. It is tempting to extend the three-dimensional method for surface waves described in Section 2.2 to interfacial flows in three dimensions. The purpose is to provide a basis for a rapid (and explicit) time-stepping scheme for 3D interfacial flows.

We consider a two-layer model with an upper layer of density ρ_2 and thickness h_2 and a lower layer of density ρ_1 and thickness h_1. Assuming that the flow may be modelled by potential theory, we introduce a velocity potential ϕ for the motion of the lower fluid, and ψ for the motion of the upper. Relevant to oceanic conditions we invoke the Boussinesq limit, i.e. $(\rho_1 - \rho_2)/\rho_1 \ll 1$. The boundary condition at the free surface may then be approximated by the rigid wall condition. The rigid wall condition also applies at the bottom of the lower fluid. The kinematic and dynamic boundary conditions at the interface at $y = \eta$ read

$$\eta_t - V = 0, \tag{20}$$

$$(\tilde{\phi} - \tilde{\psi})_t + g'\eta + \frac{|\nabla\tilde{\phi}|^2 - |\nabla\tilde{\psi}|^2 - 2V\nabla\eta\cdot\nabla(\tilde{\phi} - \tilde{\psi})}{2(1 + |\nabla\eta|^2)} + \frac{|\nabla\eta\times\nabla\tilde{\phi}|^2 - |\nabla\eta\times\nabla\tilde{\psi}|^2}{2(1 + |\nabla\eta|^2} = 0, \tag{21}$$

where $V = \phi_n\sqrt{1 + |\nabla\eta|^2}$ denotes a scaled normal velocity of the interface, a tilde means the value of the quantity at the actual position of the interface and $g' = g(\rho_1 - \rho_2)/\rho_1$.

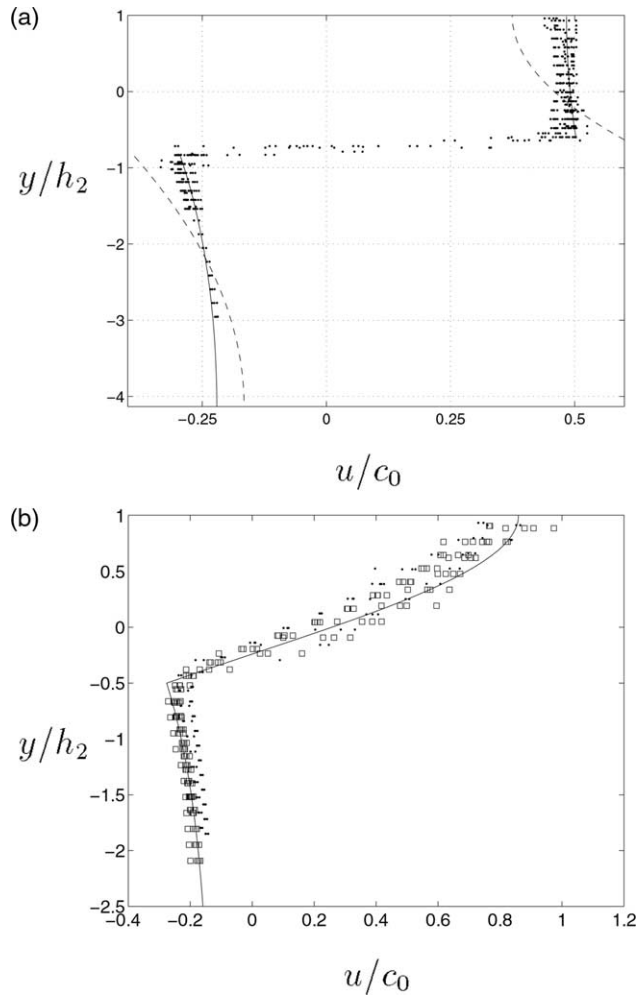

Fig. 9. Velocity profiles due to internal solitons. (a) Two-layer fluid with $A/h_2 = 0.78$. (b) Fluid with an upper shallow layer with a linear stratification and lower deep layer with constant density, $A/h_2 = 0.5$. c_0 denotes the linear long wave speed of the medium (different in the two cases). Fully nonlinear computations (solid line), KdV model (dashed line), experiments (dots, squares). $h_1/h_2 = 4.13$. From Refs. [43,53]. Reproduced with permission by J Fluid Mech.

The prognostic equations (20) and (21) may be integrated once relations between $(\tilde{\phi} + \tilde{\psi}, V)$ and $(\tilde{\phi} - \tilde{\psi}, \eta)$ are obtained. The latter may be derived using Green's theorem, giving for the upper and lower layer, respectively

$$\iint_S \left(\frac{1}{r} + \frac{1}{r_2}\right)\frac{\partial \psi'}{\partial n'}\mathrm{d}S = -2\pi\tilde{\psi} + \iint_S \tilde{\psi}'\frac{\partial}{\partial n'}\left(\frac{1}{r} + \frac{1}{r_2}\right)\mathrm{d}S, \tag{22}$$

$$\iint_S \left(\frac{1}{r} + \frac{1}{r_1}\right)\frac{\partial \phi'}{\partial n'}\mathrm{d}S = 2\pi\tilde{\phi} + \iint_S \tilde{\phi}'\frac{\partial}{\partial n'}\left(\frac{1}{r} + \frac{1}{r_1}\right)\mathrm{d}S, \tag{23}$$

where $r_2^2 = R^2 + (\eta' + \eta - 2h_2)^2$ and $r_1^2 = R^2 + (\eta' + \eta + 2h_1)^2$. The normal vector $\mathbf{n}$ is pointing out of the lower fluid and into the upper fluid.

The first part of the integral on the left of Eq. (22) is evaluated as described in Section 2.2. In the second part of the integral we first replace $1/r_2$ by $1/R_2 + (\eta' + \eta)(2h_2/R_2^3)$, where $R_2^2 = R^2 + (2h_2)^2$. The remaining part is moved to the right of the equation. Thus we evaluate

$$\frac{1}{2\pi}\mathscr{F}\left(\iint_{-\infty}^{\infty} W'\left(\frac{1}{R_2} + \frac{2(\eta' + \eta)h_2}{R_2^3}\right)\mathrm{d}\mathbf{x}'\right) = \frac{e_2}{k}\mathscr{F}(W) + e_2\mathscr{F}(\eta W) + \mathscr{F}(\eta\mathscr{F}^{-1}(e_2\mathscr{F}(W))), \tag{24}$$

where $W = \tilde{\psi}_n\sqrt{1 + |\nabla\eta|^2}$ and $e_2 = \mathrm{e}^{-2kh_2}$ are introduced. In a similar procedure for Eq. (23) we evaluate

$$\frac{1}{2\pi}\left(\mathscr{F}\iint_{-\infty}^{\infty} V'\left(\frac{1}{R_1} - \frac{2(\eta' + \eta)h_1}{R_1^3}\right)\mathrm{d}\mathbf{x}'\right) = \frac{e_1}{k}\mathscr{F}(V) - e_1\mathscr{F}(\eta V) - \mathscr{F}(\eta\mathscr{F}^{-1}(e_1\mathscr{F}(V))), \tag{25}$$

where $V = \tilde{\phi}_n\sqrt{1 + |\nabla\eta|^2}$ and $e_1 = \mathrm{e}^{-2kh_1}$.

The first part of the integral on the right of Eq. (23) is evaluated as described in Section 2.2. For the second integral we obtain

$$\frac{1}{2\pi}\mathscr{F}\left(\iint_S \tilde{\phi}'\frac{\partial}{\partial n'}\frac{1}{r_1}\mathrm{d}S\right) = -e_1\mathscr{F}(\tilde{\phi}) + \mathscr{F}\{\eta\mathscr{F}^{-1}(ke_1\mathscr{F}(\tilde{\phi})\}) - \frac{i\mathbf{k}}{k}e_1\cdot\mathscr{F}(\eta\nabla\tilde{\phi}) + \mathscr{F}(T_1(\tilde{\phi})), \tag{26}$$

where $T_1(\tilde{\psi})$ is obtained below in Eq. (30). A similar result holds for $\int\int_S \tilde{\phi}'(\partial(1/r_2)/\partial n')\mathrm{d}S$ on the right of Eq. (22), except that a plus sign appears in front of the term corresponding to the first term on the left of Eq. (26).

The Fourier transformed equation (22) becomes

$$\begin{aligned}\mathscr{F}(W) = {} & -kE_2\mathscr{F}(\tilde{\psi}) + kE_2\mathscr{F}(\eta W_1) - \mathrm{i}\mathbf{k}\cdot\mathscr{F}(\eta\nabla\tilde{\psi}) \\ & + kC_2[\mathscr{F}(T(\tilde{\psi}) + T_2(\tilde{\psi})) + \mathscr{F}(N(W) \\ & + N_2(W))] - kC_2[e_2\mathscr{F}(\eta(W - W_1)) \\ & + \mathscr{F}(\eta\mathscr{F}^{-1}(e_2\mathscr{F}(W - W_1)))],\end{aligned} \tag{27}$$

where we have introduced $E_2 = (1 - e_2)/(1 + e_2)$, $C_2 = 1/(1 + e_2)$ and $\mathscr{F}(W_1) = -kE_2\mathscr{F}(\tilde{\psi})$. Furthermore, T and N are given by Eqs. (9) and (10), respectively, and T_2 and N_2 are obtained below, from Eqs. (30) and (29), respectively.

Fourier transform of Eq. (23) gives, similarly,

$$\mathscr{F}(V) = kE_1\mathscr{F}(\tilde{\phi}) - kE_1\mathscr{F}(\eta V_1) - \mathrm{i}\mathbf{k}\cdot\mathscr{F}(\eta\nabla\tilde{\phi}) + kC_1[\mathscr{F}(T(\tilde{\phi}) + T_1(\tilde{\phi})) + \mathscr{F}(N(V) + N_1(V))] + kC_1[e_1\mathscr{F}(\eta(V - V_1)) + \mathscr{F}(\eta\mathscr{F}^{-1}(e_1\mathscr{F}(V - V_1)))], \tag{28}$$

where $E_1 = (1 - e_1)/(1 + e_1)$, $C_1 = 1/(1 + e_1)$ and $\mathscr{F}(V_1) = kE_1\mathscr{F}(\tilde{\phi})$. Finally, T_1 and N_1 are given by

$$N_1(V) = \frac{1}{2\pi}\int\int_{-\infty}^{\infty} V'\left(\frac{1}{R_1} - \frac{2(\eta' + \eta)h_1}{R_1^3} - \frac{1}{r_1}\right)\mathrm{d}\mathbf{x}', \tag{29}$$

$$T_1(\tilde{\phi}) = \frac{1}{2\pi}\int\int_{-\infty}^{\infty} \tilde{\phi}'\frac{12h_1^2(\eta' + \eta)}{R_1^5}\mathrm{d}\mathbf{x}' + \frac{1}{2\pi}\int\int_{-\infty}^{\infty} \times\tilde{\phi}'(\mathbf{R}\cdot\nabla\eta - (\eta + \eta') - 2h_1)\left(\frac{1}{r_1^3} - \frac{1}{R_13}\right)\mathrm{d}x'. \tag{30}$$

N_2 is obtained from Eq. (29) by replacing h_1 by $-h_2$, r_1 by r_2, R_1 by R_2 and V by W. T_2 is obtained similarly from Eq. (30).

It is convenient to introduce the sum $\tilde{\Phi} = \tilde{\phi} + \tilde{\psi}$ and the difference $\tilde{\Psi} = \tilde{\phi} - \tilde{\psi}$ into Eqs. (27) and (28). In order to integrate Eqs. (20) and (21), the sum $\tilde{\Phi}$ and the vertical velocity $V = W$ at the interface are required, given $\tilde{\Psi}$ and η. Subtracting Eq. (27) from Eq. (28), using that $V - W = 0$, gives

$$\begin{aligned}(E_1 + E_2)\mathscr{F}(\tilde{\Phi}) &= -(E_1 - E_2)\mathscr{F}(\tilde{\Psi}) + 2E_2\mathscr{F}(\eta W_1) + 2E_1\mathscr{F}(\eta V_1) \\ &+ 2\mathrm{i}\frac{\mathbf{k}}{k}\cdot\mathscr{F}(\eta\nabla\tilde{\Psi}) - (C_1 - C_2)\mathscr{F}(T(\tilde{\Phi})) \\ &- (C_1 + C_2)\mathscr{F}(T(\tilde{\Psi})) - (C_1 - C_2)\mathscr{F}(\tfrac{1}{2}(T_1(\tilde{\Phi}) \\ &+ T_2(\tilde{\Phi})) - (C_1 + C_2)\mathscr{F}(\frac{1}{2}(T_1(\tilde{\Phi}) - T_2(\tilde{\Phi})) \\ &- (C_1 - C_2)\mathscr{F}(\frac{1}{2}(T_1(\tilde{\Psi}) - T_2(\tilde{\Psi})) \\ &- (C_1 + C_2)\mathscr{F}(\frac{1}{2}(T_1(\tilde{\Psi}) + T_2(\tilde{\Psi})) \\ &- 2(C_1 - C_2)\mathscr{F}(N(V)) - 2[C_1\mathscr{F}(N_1(V)) \\ &- C_2\mathscr{F}(N_2(V))] - 2C_1[e_1\mathscr{F}(\eta(V - V_1)) \\ &+ \mathscr{F}(\eta\mathscr{F}^{-1}(e_1\mathscr{F}(V - V_1)))] - 2C_2[e_2\mathscr{F}(\eta(V - W_1)) \\ &+ \mathscr{F}(\eta\mathscr{F}^{-1}(e_2\mathscr{F}(V - W_1)))],\end{aligned} \tag{31}$$

where $\mathscr{F}(W_1) = -(1/2)kE_2(\mathscr{F}(\tilde{\Phi}) - \mathscr{F}(\tilde{\Psi}))$ and $\mathscr{F}(V_1) = (1/2)kE_1(\mathscr{F}(\tilde{\Phi}) + \mathscr{F}(\tilde{\Psi}))$.

Similarly, adding Eqs. (27) and (28) gives

$$\begin{aligned}2\mathscr{F}(V) &= \tfrac{1}{2}k(E_1 - E_2)\mathscr{F}(\tilde{\Phi}) + \tfrac{1}{2}k(E_1 + E_2)\mathscr{F}(\tilde{\Psi}) \\ &+ kE_2\mathscr{F}(\eta W_1) - kE_1\mathscr{F}(\eta V_1) - \mathrm{i}\mathbf{k}\cdot\mathscr{F}(\eta\nabla\tilde{\Phi}) \\ &+ \tfrac{1}{2}k(C_1 + C_2)\mathscr{F}(T(\tilde{\Phi})) + \tfrac{1}{2}k(C_1 - C_2)\mathscr{F}(T(\tilde{\Psi})) \\ &+ \tfrac{1}{2}k(C_1 + C_2)\mathscr{F}(\tfrac{1}{2}(T_1(\tilde{\Phi}) + T_2(\tilde{\Phi})) \\ &+ \tfrac{1}{2}k(C_1 + C_2)\mathscr{F}(\frac{1}{2}(T_1(\tilde{\Psi}) - T_2(\tilde{\Psi})) \\ &+ \tfrac{1}{2}k(C_1 - C_2)\mathscr{F}(\tfrac{1}{2}(T_1(\tilde{\Phi}) - T_2(\tilde{\Phi})) \\ &+ \tfrac{1}{2}k(C_1 - C_2)\mathscr{F}(\tfrac{1}{2}(T_1(\tilde{\Psi}) + T_2(\tilde{\Psi})) \\ &+ k(C_1 + C_2)\mathscr{F}(N(V)) + k[C_1\mathscr{F}(N_1(V)) \\ &+ C_2\mathscr{F}(N_2(V))] + kC_1[e_1\mathscr{F}(\eta(V - V_1)) \\ &+ \mathscr{F}(\eta\mathscr{F}^{-1}(e_1\mathscr{F}(V - V_1)))] \\ &- kC_2[e_2\mathscr{F}(\eta(V - W_1)) \\ &+ \mathscr{F}(\eta\mathscr{F}^{-1}(e_2\mathscr{F}(V - W_1)))].\end{aligned} \tag{32}$$

6.1. Infinite depth

In the case when $h_1, h_2 \to \infty$, we have that $E_1, E_2, C_1, C_2 \to 1$, and the equations for $\tilde{\Phi}$ and V simplify to

$$\mathscr{F}(\tilde{\Phi}) = \mathscr{F}(\eta(V_1 + W_1)) + \mathrm{i}\frac{\mathbf{k}}{k}\cdot\mathscr{F}(\eta\nabla(\tilde{\Psi})) - \mathscr{F}(T(\tilde{\Psi})), \tag{33}$$

$$2\mathscr{F}(V) = k\mathscr{F}(\tilde{\Psi}) - k\mathscr{F}(\eta(V_1 - W_1)) - \mathrm{i}\mathbf{k}\cdot\mathscr{F}(\eta\nabla(\tilde{\Phi})) + k\mathscr{F}(T(\tilde{\Phi})) + 2k\mathscr{F}(N(V)). \tag{34}$$

Eqs. (31) and (32), or alternatively Eqs. (33) and (34), may be solved applying the method of successive approximations. This provides explicit approximations to V and $\tilde{\Phi}$ similar to the equations in Section 2.2. Any accuracy may be achieved by a continued iteration. The integrals (29) and (30) have rapidly decaying kernels. For the former we have, to leading order, $N_1(V) \sim \int\int \mathscr{O}(V\eta^2R_1^{-5})\mathrm{d}\mathbf{x}'$, while for the latter $T_1(\tilde{\phi}) \sim \int\int \mathscr{O}(\tilde{\phi}\eta^2R_1^{-5})\mathrm{d}\mathbf{x}'$. Similar results hold for N_2 and T_2. This means that the contributions to the integrals are very local, and the integration may be truncated.

6.2. Single layer

In the case when there is only one layer we obtain

$$\mathscr{F}(V) = kE_1\mathscr{F}(\tilde{\phi}) - kE_1\mathscr{F}(\eta V_1) - \mathrm{i}\mathbf{k}\cdot\mathscr{F}(\eta\nabla\tilde{\phi}) + kC_1\mathscr{F}(T(\tilde{\phi}) + T_1(\tilde{\phi})) + kC_1\mathscr{F}(N(V) + N_1(V)) + kC_1(e_1\mathscr{F}(\eta(V - V_1)) + \mathscr{F}(\eta\mathscr{F}^{-1}(e_1\mathscr{F}(V - V_1)))). \quad (35)$$

This gives the extension of the method to a single layer fluid of finite depth.

7. Concluding remarks

Some recent developments on the formation of extreme waves, kinematics of steep waves, the phenomenon of ringing and currents in the ocean induced by internal waves are reviewed.

Formation of extreme waves are simulated by means of a rapid fully nonlinear model. A large wave event taking place in a wave group is characterized by an elevation being significantly larger than the initial amplitude of the group. A significant portion of the wave energy is transferred to high wavenumbers during the event, but is returned to the main part of the wave spectrum afterwards, indicating that recurrence is taking place.

PIV represents an invaluable experimental tool to analyse the kinematics of waves. PIV measurements and theoretical analysis of Stokes waves exhibit an exponential velocity profile. Results are here shown for kA up to 0.16, k the wavenumber, A the amplitude. The non-dimensional velocity profile under crest of an extreme wave is also very close to an exponential profile. Computations with $k\eta_{\mathrm{m}}$ up to 0.34 shows this result, η_{m} the maximal elevation of the wave event.

Experimental results of the horizontal force on a vertical circular cylinder in steep waves have been summarized. A secondary cycle of high frequency may occur in the force history experienced by a vertical cylinder in long waves. The secondary force cycle typically occurs beyond a threshold amplitude. The presence of the secondary force cycle is observed for a wave longer than about 10 times the cylinder diameter and a Froude number $\omega\eta_{\mathrm{m}}/\sqrt{gD}$ larger than about 0.4, ω the wave frequency, g the acceleration of gravity, D the cylinder diameter. The higher harmonic force may significantly enhance a tuned build-up of resonant motions of marine structures.

Weakly and fully nonlinear models of internal solitons are discussed. Properties of the waves and the resulting induced fluid velocity are exemplified. The fluid velocity close to the ocean surface may become comparable to the wave speed when the upper shallow fluid layer has a linear stratification. This is true even for moderate wave amplitude.

A rapid scheme for fully nonlinear interfacial waves in three dimensions is finally derived. The method of successive approximations provides an explicit approximation to the solution of the Laplace equation governing the fluid flow. The formulae complement the rapid model of free surface flows in three dimensions, described in Ref. [9]. The schemes may be useful for simulations of various wave phenomenae taking place on the ocean surface and at a thermocline in the ocean.

Acknowledgements

This review lecture was held at the LABMATH Symposium at Institute Teknologi Bandung, Indonesia, 7–9th September, 2001. The author expresses his gratitude to Drs Andonowati and E. Soewono of ITB, the hosts of the meeting. The access to laboratory data on 'ringing' by Professors J.R. Chaplin and T. Marthinsen, and the assistance and suggestions by Drs D. Clamond, M. Huseby, A. Jensen and K. Trulsen during the preparation of the paper are gratefully acknowledged. This work was conducted under the Strategic University Programme 'General Analysis of Realistic Ocean Waves' funded by the Research Council of Norway.

References

[1] ISSC 2000. Report of the Environment Committee. 14th International Ship and Offshore Structural Congress 1, Nagasaki, Japan.
[2] Rogue. Waves Workshop. IFREMER, Brest, 29–30 November 2000.
[3] Dysthe KB. Note on a modification to the nonlinear Schrödinger equation for application to deep water. Proc R Soc Lond 1979;A369:105.
[4] Yuen HC, Lake BM. Nonlinear dynamics of deep-water gravity waves. Adv Appl Mech 1982;22:67.
[5] Trulsen K, Kliakhandler I, Dysthe KB, Velarde MG. On weakly nonlinear modulation of waves on deep water. Phys Fluids 2000;12(10):2432.
[6] Dommermuth D, Yue DKP. A high-order spectral method for the study of nonlinear gravity waves. J Fluid Mech 1987;184:267.
[7] West BJ, Brueckner KA, Janda RS, Milder DM, Milton RL. A new numerical method for surface hydrodynamics. J Geophys Res 1987;92(11):11803.
[8] Yasuda T, Mori N. High order nonlinear effects on deep-water random wave trains. Proceedings of the International Symposium: waves—physics and numerical modelling. Vancouver, Canada: University of British Columbia; 1994. p. 823–32.
[9] Clamond D, Grue J. A fast method for fully nonlinear water wave computations. J Fluid Mech 2001;447:337.
[10] Dold JW, Peregrine DH. Water-wave modulation. Proceedings of the 20th International Conference on Coastal Engineering. American Society of Civil Engineering, Taipei, 10–14 November 1986. p. 163.
[11] Banner ML, Tian X. On the determination of the onset of breaking for modulating surface water waves. J Fluid Mech 1998;367:107.
[12] Zakharov VE. Stability of periodic wave of finite amplitude on the surface of a deep fluid. J Appl Mech Phys, Engl Transl 1968;2:190.

[13] Clamond D, Grue J. On an efficient numerical model for freak wave simulations. Proceedings of the 11th International Offshore and Polar Engineering Conference and Exhibition, ISOPE 2001, Stavanger, Norway, 17–22 June 2001.
[14] Tørum A, Gudmestad OT, editors. Water wave kinematics. NATO ASI Series. Dordrecht: Kluwer Academic Publishers; 1990. 771 pp.
[15] Baldock TE, Swan C, Taylor PH. A laboratory study of nonlinear surface waves on water. Proc R Soc Lond, A 1996;354:649.
[16] Huseby M, Grue J. An experimental investigation of higher-harmonic wave forces on a vertical cylinder. J Fluid Mech 2000;414:75.
[17] Sveen JK. An introduction to MatPIV v.1.1. Documentation and code; 1998. http://www.math.uio.no~jks.
[18] Jensen A, Sveen JK, Grue J, Richon J-B, Gray C. Accelerations in water waves by extended particle image velocimetry. Exp Fluids 2001;30:500.
[19] Finne S, Grue J. On the complete radiation–diffraction problem and wave-drift damping of marine bodies in the yaw mode of motion. J Fluid Mech 1998;357:289.
[20] Newman JN, Lee C-H. Boundary-element methods in offshore structure analysis. Proceedings of the 20th International Conference on Offshore Mechanic and Arctic Engineering. OMAE'01, 3–8 June 2001, Rio de Janeiro, Brazil. p. 1–13.
[21] Ringing Report 1993. Higher order wave load effects on large volume structures. Task 2: Interpretation of existing measurements-Project Memo. MT51-F93-0100. Marintek Sintef Group, Norway.
[22] Langen I, Skjåstad O, Haver S. Measured and predicted dynamic behaviour of an offshore gravity platform. Appl Ocean Res 1998; 20:15.
[23] Grue J, Bjørshol G, Strand Ø. Higher harmonic wave exciting forces on a vertical cylinder. Department of Mathematics, University of Oslo, Preprint 2; 1993. ISBN 82-553-0862-8.
[24] Grue J, Bjørshol G, Strand Ø. Nonlinear wave loads which may generate 'ringing' responses of offshore structures. Ninth International Workshop on Water Waves and Floating Bodies, 17–20 April 1994, Kyushu, Japan. p. 55.
[25] Stansberg CT, Huse E, Krokstad JR, Lehn E. Experimental study of nonlinear loads on vertical cylinders in steep random waves. Proceedings of the 5th ISOPE Conference, I, ISOPE, Golden, CO, USA; 1995. p. 75–82.
[26] Chaplin JR, Rainey RCT, Yemm RW. Ringing of a vertical cylinder in waves. J Fluid Mech 1997;350:119.
[27] Scolan Y-M, Le Boulluec M, Chen X-B, Deleuil G, Ferrant P, Malenica S, Molin B. Some results from numerical and experimental investigations on the high frequency responses of offshore structures. Behaviour of Offshore. Structural Conference, BOSS'97; 1997.
[28] Faltinsen OM, Newman JN, Vinje T. Nonlinear wave loads on a slender vertical cylinder. J Fluid Mech 1995;289:179–99.
[29] Malenica S, Molin B. Third-harmonic wave diffraction by a vertical cylinder. J Fluid Mech 1995;302:203.
[30] Ferrant P. Fully nonlinear interactions of long-crested wave packets with a three dimensional body. 22nd ONR Symposium in Nav. Hydrod., Washington, DC Tue/Wed Sess. Prov. Proc.; 1998. p. 59–72.
[31] Huseby M. Experiments on ringing loads and higher harmonic wave forces. Dr. Scient. Thesis. Faculty of Math. Nat. Sci., Univ. of Oslo; 2000. 47 pp.
[32] Model test report for Saga Petroleum. Higher order wave loads on a vertical column. MT51-F95-0139. Marintek Sintef Group, Norway; 1995.
[33] Sarpkaya T. Force on a circular cylinder in viscous oscillatory flow at low Keulegan-Karpenter numbers. J Fluid Mech 1986;165:61.
[34] Farmer DM, Smith JD. Tidal interaction of stratified flow with a sill in Knight Inlet. Deep-Sea Res 1980;27A:239.
[35] Apel JR, Holbrook JR, Liu AK, Tsai J. The Sulu Sea internal soliton experiment. J Phys Oceanogr 1985;15:1625.
[36] Pingree RD, Mardell GT. Solitary internal waves in the Celtic Sea. Prog Oceanogr 1985;14:431.
[37] Stanton TP, Ostrovsky LA. Observations of highly nonlinear internal solitons over the continental shelf. Geophys Rev Lett 1998;25:2695.
[38] Keulegan GH. Characteristics of internal solitary waves. J Res Natl Bur Stand 1953;51:133.
[39] Long RR. Solitary waves in one and two fluid systems. Tellus 1956;8: 460.
[40] Koop CG, Butler G. An investigation on internal solitary waves in a two-fluid system. J Fluid Mech 1981;112:225.
[41] Segur H, Hammack JL. Soliton models of long internal waves. J Fluid Mech 1982;118:285.
[42] Kao TW, Pan F-S, Renouard D. Internal solitons on the pycnocline: generation, propagation, and shoaling and breaking over a slope. J Fluid Mech 1985;159:19.
[43] Grue J, Jensen A, Rusås P-O, Sveen JK. Properties of large amplitude internal waves. J Fluid Mech 1999;380:257.
[44] Benjamin TB. Internal waves of permanent form in fluids of great depth. J Fluid Mech 1967;29:559.
[45] Ono H. Algebraic solitary waves in stratified fluids. J Phys Soc Jpn 1975;39:1082.
[46] Joseph RI. Solitary waves in a finite depth fluid. J Phys A: Math Gen 1977;10:L225.
[47] Kubota T, Ko DRS, Dobbs LD. Weakly-nonlinear, long internal gravity waves in stratified fluids of finite depth. J Hydronaut 1978;12: 157.
[48] Miloh T. On periodic and solitary wavelike solutions of the intermediate long-wave equation. J Fluid Mech 1990;211:617.
[49] Amick CJ, Turner REL. A global theory of internal solitary waves in two-fluid systems. Trans Am Math Soc 1986;298:431.
[50] Turner REL, Vanden-Broeck J-M. The limiting configuration of interfacial gravity waves. Phys Fluids 1986;29:372.
[51] Evans WAB, Ford MJ. An integral equation approach to internal (2-layer) solitary waves. Phys Fluids 1996;8:2032.
[52] Rusås P-O. IW2 (Two-layer Internal Waves), version 1.0; 2000. http://bukharin.hiof.no/~por/internalwaves/.
[53] Grue J, Jensen A, Rusås P-O, Sveen JK. Breaking and broadening of internal solitary waves. J Fluid Mech 2000;413:181.
[54] Roberts AJ. A stable and accurate numerical method to calculate the motion of a sharp interface between fluids. IMA J Appl Math 1983;31:31.
[55] Eliassen A, Fjørtoft R. The interface method for calculating the temporal evolution of a two-fluid system. Fronters Sci, Ann NY Acad Sci 1992;661:54.
[56] Grue J, Friis A, Palm E, Rusås P-O. A method for computing unsteady fully nonlinear interfacial waves. J Fluid Mech 1997;351: 223.